Emerging antiferroelectric phases with fascinating dielectric, polarization and strain response in NaNbO$_3$-(Bi$_{0.5}$Na$_{0.5}$)TiO$_3$ lead-free binary system

He Qi [a], Aiwen Xie [a], Jian Fu [a], Ruzhong Zuo [b],*

[a] *Institute of Electro Ceramics & Devices, School of Materials Science and Engineering, Hefei University of Technology, Hefei, 230009, P.R. China*
[b] *School of Materials Science and Engineering, Anhui Polytechnic University, Wuhu, 241000, P.R. China*

A B S T R A C T

Environmentally-benign antiferroelectrics (AFEs) have attracted a great deal of attention in recent years owing to their special structure and polarization/strain-electric field response, exhibiting giant application advantages in multifunctional devices. In this work, a detailed phase diagram in a binary lead-free system between AFE NaNbO$_3$ (NN) and ferroelectric (FE) (Bi$_{0.5}$Na$_{0.5}$)TiO$_3$ (BNT) was established according to the measurement of dielectric and ferroelectric properties in combination with the multiscale structure analysis such as Raman spectra, synchrotron x-ray diffraction and transmission electron microscopy. Multiple AFE phases of different stability, crystal symmetry and domain morphology were stabilized near room temperature, involving AFE orthorhombic P (*Pbma*) and R (*Pnma*) phases in NN-rich compositions and AFE tetragonal phase (*P4bm*) in BNT-rich compositions, as well as field induced metastable AFE monoclinic phase (*P2$_1$*). Owing to the electric field induced AFE-FE phase transformation especially for relaxor AFEs with antipolar nanoregions, tunable and excellent electrical properties of temperature-stable dielectric permittivity, ultrahigh energy-storage density and efficiency and low-hysteresis high strain can be generated in the proximity of these AFEs, showing outstanding potentials in thermally-stable capacitors, dielectric energy storage and large-strain ceramic actuators for NN-BNT solid solutions.

© 2021 Acta Materialia Inc. Published by Elsevier Ltd. All rights reserved.

1. Introduction

Antiferroelectrics (AFEs) exhibit typical double polarization-electric field (*P-E*) and corresponding large strain due to field induced AFE-ferroelectric (FE) phase transition, providing a solid foundation for important engineering applications in digital displacement transducers, energy storage capacitors, electrocaloric cooling devices, and flat panel displays [1–5]. Therefore, the AFE materials, particularly lead-free AFE counterparts have achieved widespread attention in recent years since proposed in 1951 [6].

AFE structure has been widely reported in (Bi$_{1/2}$Na$_{1/2}$)TiO$_3$ (BNT) [7–13], NaNbO$_3$ (NN) [5,14,15] and AgNbO$_3$ (AN) [16–19] based lead-free perovskites, in which pure NN and AN are thought to be typical lead-free AFEs. NN is a well-documented AFE perovskite compound with a complex sequence of polymorphic phase transition with temperature, in which at least two kinds of AFEs with *Pbma* (P phase) and *Pnma* (R phase) space groups

were reported in a wide temperature range of -100~480 °C, as shown in Fig. 1a [20–22]. However, the AFE P phase in pure NN ceramic at room temperature usually irreversibly transforms into an FE state under a large driving field of ~9 kV/mm, leading to a square *P-E* loop after the first-cycle loop [23–25]. Lots of attempts have been made to enhance the stability of the AFE P phase or stabilize the high-temperature AFE R phase close to room temperature by adding other ABO$_3$ perovskites with lower tolerance factor or lower polarizability [5,15,26–28]. Similar to NN, typical double *P-E* loops as well as excellent energy-storage properties were obtained in AN-based solid solutions [16–18]. However, the high cost of Ag would largely limit its further usage in industry.

Pure BNT shown in Fig. 1b was reported to have a phase transition from high-temperature prototypic cubic phase (Pm-3m) to an AFE tetragonal (AFE$_T$) phase with *P4bm* space group at ~540 °C, which possesses an unusual combination of in-phase oxygen-octahedral tilts (Glazer notation $a^0a^0c^+$ [29]) and anti-parallel cation displacements along the polar axis [8]. The FE and AFE phases in BNT exhibit large spontaneous polarization and obvious dielectric relaxation behavior, thus leading to excellent energy storage and electrostrain behavior [9–11,30]. Local AFE components
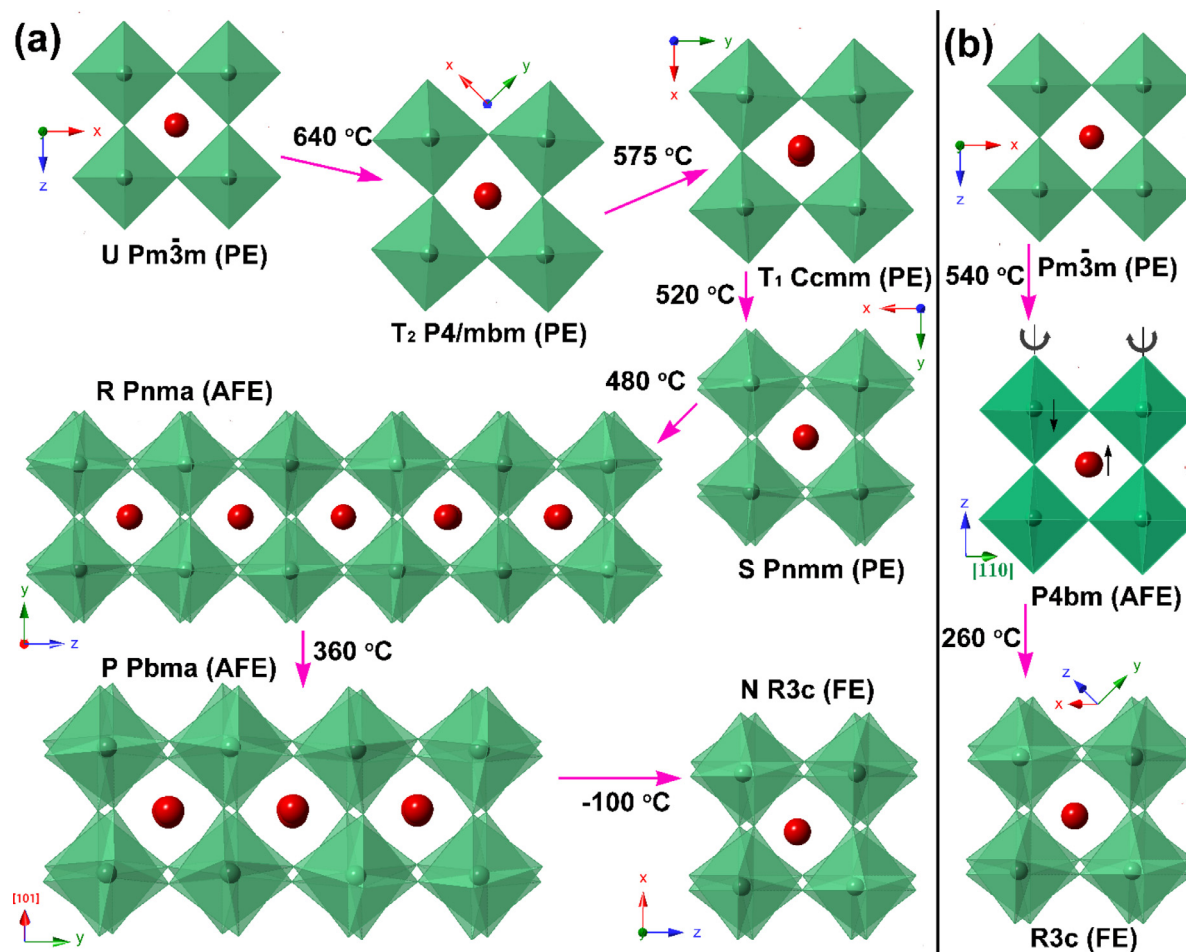
Fig. 1. Crystal structure models for (a) NN and (b) BNT ceramics under different temperatures.

(i.e. intergrown microstructure) have also been reported in BNT at room temperature, and the fraction of such components increases with increasing temperature [13]. Yet, it is difficult to identify the AFE structure in BNT-based ceramic from the measurement of average structure and polarization-field response owing to the strong dielectric relaxation behavior.

Previous studies indicated that 0.76NN-0.24BNT and 0.76BNT-0.24NN AFE compositions own giant advantages in energy-storage (record-high energy-storage density W_{rec}~12.2 J/cm^3 for bulk ceramic capacitors) and electrostrictive properties (very large purely-electrostrictive strain of ~0.2%) [5,9,31]. Therefore, it would be very interesting to deeply explore multiple AFE phases and their structure and property characteristics in NN-BNT solid solutions through constructing a full phase diagram of this lead-free binary system. In this work, average and local structure (Raman spectrum, synchrotron X-ray diffraction (XRD) and transmission electron microscopy (TEM)), various electrical properties and the Rietveld structure refinement were employed to identify different phases and their performances.

2. Experimental

(1-x)NN-xBNT ceramics with x=0-1 were prepared by a conventional solid-state reaction method [5]. The grain morphology was observed by using a field-emission scanning electron microscope (FE-SEM, SU8020, JEOL, Tokyo, Japan). Before the SEM observation, the samples were polished and thermally etched at 1000-1150 °C for 30 min. The phase structure was analyzed by a powder x-ray diffractometer (D/Mzx-rB; Rigaku, Tokyo, Japan) with Cu $K\alpha$ radi-

ation under an acceleration condition of 40 kV and 30 mA. The full XRD data were analyzed through the Rietveld refinement using GSAS software. Raman spectra were collected at room temperature on well-polished pellets using 532 nm excitation using a Raman spectrometer (LabRam HR Evolution, HORIBA JOBIN YVON, Longjumeau Cedex, France). Dielectric properties as a function of temperature and frequency were measured by an LCR meter (Agilent E4980A, Santa Clara, CA). The domain morphology observation was performed on a field-emission transmission electron microscope (FE-TEM, JEM-2100F, JEOL, Japan) operated at 200 kV. For TEM examination, samples were first mechanically polished to a thickness of ~20 μm and then ion-milled on a Precision Ion Polishing System (PIPS, Model 691, Gatan Inc., Pleasanton, CA, USA) at 5 kV. All specimens were annealed at 80°C for at least one day to release the mechanical stress before the observation. The ferroelectric testing system (Precision Multiferroic, Radiant Technologies Inc., Albuquerque, NM) connected with a laser interferometric vibrometer (SP-S 120, SIOS Meβtechnik GmbH, Germany) were used to measure unipolar and bipolar P-E hysteresis loops and strain vs. electric field (S-E) curves. For electrical measurements, the samples with a thickness of ~0.15 mm and an electrode diameter of 3 mm were used. Synchrotron XRD measurement was carried out by high-resolution θ−2θ step-scans using a Huber 5021 six-circle diffractometer with a NaI scintillation detector on well-polished and Au-sputtered disk samples under various electric field conditions at Shanghai Synchrotron Radiation Facility (SSRF) using beam line 14B1 with a monochromatic incident beam with a wavelength close to 0.6887 Å (18 keV).

3. Results

3.1. Composition-dependent microstructure and phase structure

Fig. 2 shows the grain morphology of a few $(1-x)$NN-xBNT ceramics sintered at their optimal temperature. All samples exhibit dense and uniform microstructure. Both of pure NN and BNT ceramics exhibit relatively large grains (average grain size ~7 μm), compared with NN-BNT binary solid-solution compositions, for example, ~2-3 μm at $x=0.4$ and $x=0.6$. This is basically due to relatively low sintering temperatures for NN-BNT solid solutions.

Fig. 3a shows XRD patterns of $(1-x)$NN-xBNT ceramics at room temperature. It can be seen that all compositions exhibit a pure perovskite structure without any secondary phases. The phase structure transition can be distinguished by carefully looking at $(200)_C$ diffraction peaks (see Fig. 3b). An obvious splitting of the $(200)_C$ diffraction line together with the intensity ratio of $I_{002}/I_{200}=2:1$ suggests a typical orthorhombic phase for the pure NN ceramic ($x=0$). The substitution of BNT for NN makes $(002)_C$ and $(200)_C$ peaks gradually merge together, such that a single $(200)_C$ peak appears in the composition range of $0.16 \leq x < 0.3$. With further increasing BNT content, a tiny shoulder can be seen at the lower-degree side of $(200)_C$ diffraction lines, suggesting the appearance of a tetragonal phase. The tetragonal phase seems to exist within a wide composition range of $x=0.3-0.8$. As $x > 0.8$, the compositions should belong to an $R3c$, similar to pure BNT. Apart from the change of $(200)_C$ diffraction peaks, an obvious change in the peak intensity can be also found on the $(100)_C$, $(111)_C$ and $(210)_C$ lines, as indicated by ellipses, generally demonstrating three different phase zones within the entire composition range.

3.2. Phase transition and dielectric relaxation

The temperature dependent dielectric permittivity (ε_r) at 1 kHz for $(1-x)$NN-xBNT ceramics is shown in Figs. 4a-d. Pure NN ceramic shows an AFE orthorhombic (AFE$_O$) P phase (*Pbma* space group) at room temperature before poling. A sharp permittivity peak around T_{P-R}~365 °C should be related to the phase transition from AFE$_O$ P phase to AFE$_O$ R phase (*Pnma* space group) [21,32]. T_{P-R} value can be found to decrease monotonously with increasing the BNT content. In addition, an obvious decrease in room-temperature dielectric permittivity can be seen starting at $x=0.16$ (Fig. 4b), which is obviously related to the shift of T_{P-R} value to below room temperature [33]. The decreased dielectric permittivity behavior can also be found in pure NN ceramics with the entrance of AFE$_O$ R phase on heating, thus indicating the appearance of an AFE$_O$ R dominated phase at room temperature above $x=0.16$. A weak dielectric anomaly can be still detected at ~150 °C owing to the obvious thermal hysteresis of the P-R phase transition [33], indicating the coexistence of the AFE$_O$ R phase with a small amount of P phase at $x=0.16$. With further increasing x up to 0.18, the dielectric anomaly related to the P-R phase transition cannot be detected any
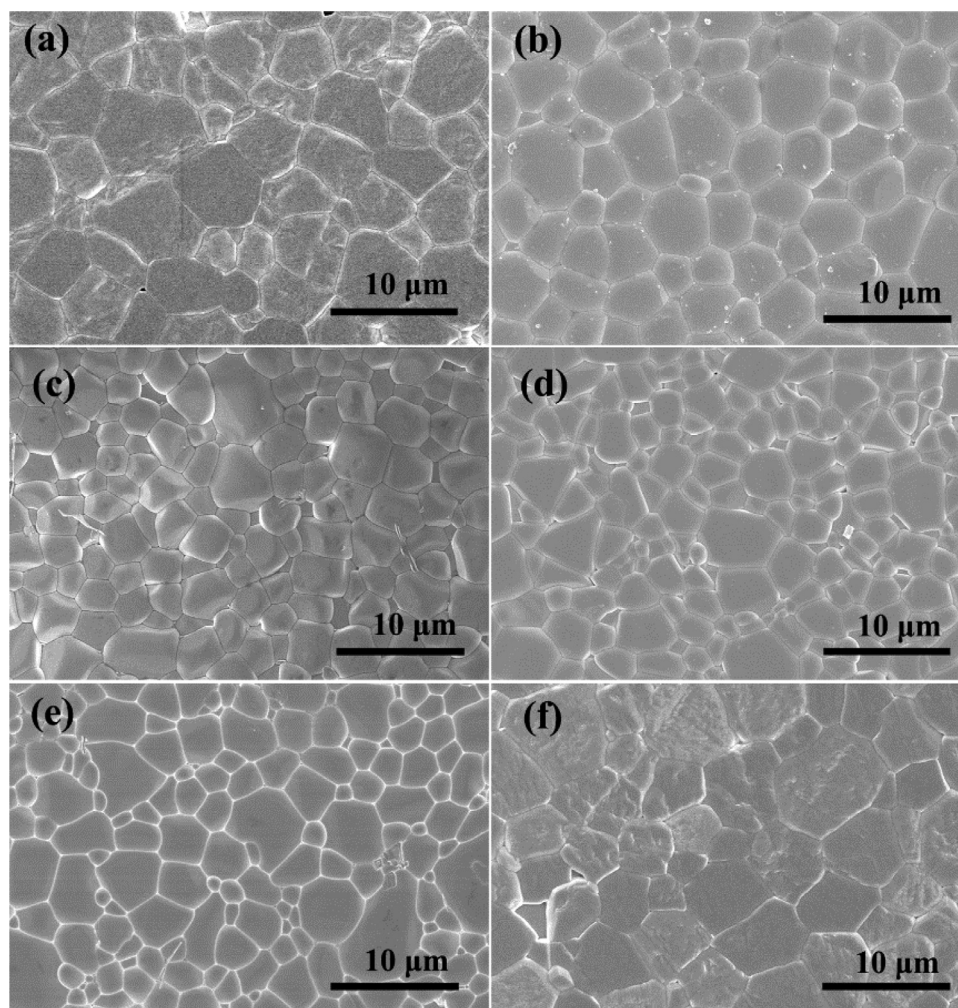

Fig. 2. SEM micrographs of polished cross-sections after thermal etching of $(1-x)$NN-xBNT ceramics sintered at optimal temperature: (a) $x=0$, (b) $x=0.2$, (c) $x=0.4$, (d) $x=0.6$, (e) $x=0.8$ and (f) $x=1$.
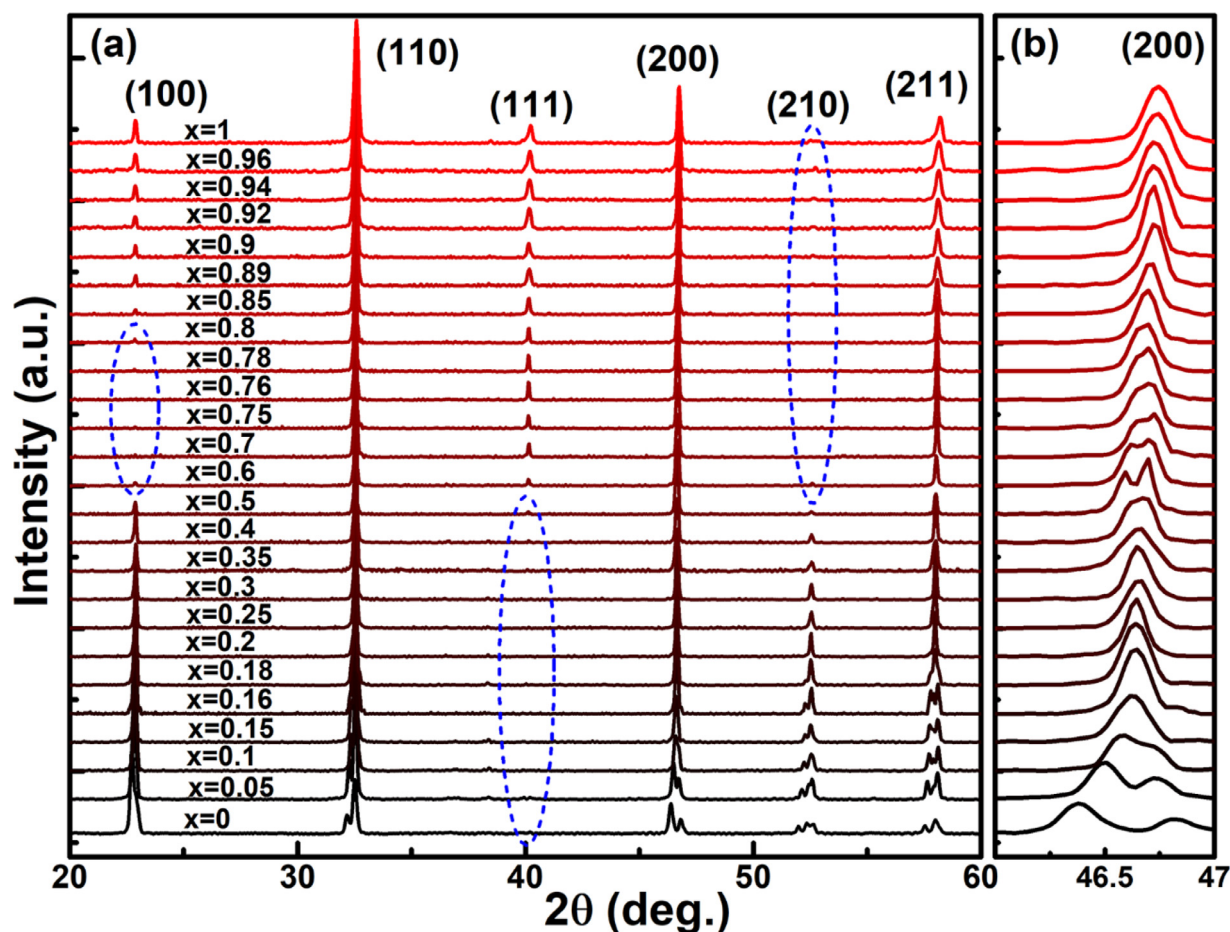
Fig. 3. (a) XRD patterns of (1-*x*)NN-*x*BNT ceramics and (b) the locally enlarged *(200)$_C$* diffraction peaks.

more above room temperature, indicating a pure AFE$_O$ R phase at room temperature. Moreover, an obvious dielectric relaxation can be seen as *x*≥0.2, as shown in Fig. 4e using the *x*=0.25 sample as an example. The reduction of the P-R phase transition temperature leads to a gradual decrease in room-temperature dielectric permittivity. The minimum permittivity value at room temperature can be found approximately at *x*=0.5, as shown in the inset of Fig. 4e. The increase of room-temperature dielectric permittivity in the BNT-rich compositions (*x*>0.5) (Fig. 4e) probably suggests the entrance into a new phase zone (AFE *P4bm* phase). It is known that pure BNT exhibits an *R3c* to *P4bm* phase transformation at T_{R-T}~260 °C, causing an obvious dielectric anomaly, as shown in Fig. 4d [34]. The T_{R-T} value decreases linearly with increasing the NN content in BNT-NN solid solutions and drops below room temperature when NN content reaches up to 20% (*x*≤0.8), so that the sample exhibits an AFE *P4bm* phase at room temperature. Owing to the dielectric relaxation characteristics of the *P4bm* phase, nearly horizontal permittivity vs. temperature curves can be obtained in the composition range of 0.5<*x*<0.8 (Fig. 4c). By comparison, the *x*>0.8 compositions should belong to an *R3c* phase at room temperature. The dielectric permittivity as a function of temperature and frequency for poled (1-*x*)NN-*x*BNT ceramics with 0.92≤*x*≤1 is shown in Fig. 4f. An obvious dielectric anomaly at T_{F-R}'~160 °C can be seen in pure BNT ceramic after poling at room temperature. This should be ascribed to the phase transition of the electric field induced FE phase into ergodic relaxor FE phase transition during heating, suggesting a nonergodic relaxor FE state at room temperature in the virgin BNT sample. With increasing NN content, the T_{F-R}' decreases monotonously and cannot be detected above room

temperature at *x*<0.92, indicating the nonergodic to ergodic relaxor FE phase transition approximately at *x*=0.9.

3.3. Characterization of average and local structures

In order to further quantitatively analyze the phase structure, the Rietveld refinement was carried out on full profiles of XRD patterns. All possible space groups in NN and BNT ceramics and their mixtures were attempted for each composition, and the optimum fitting results are shown in Fig. 5. The refined structure parameters and various agreement factors are listed in Table 1. The fit between the observed and calculated profiles is satisfactory for all the studied compositions, as confirmed by the reliability factors of weighted patterns (R_{wp}), the reliability factors of patterns (R_p), and the goodness-of-fit indicator (χ^2) in the range of 6.68-8.21%, 5.12-6.37%, and 1.25-1.96, respectively. The slightly high R_{wp} and R_p values might be related to the existence of mismatched local structures, such as a fine scale intergrown microstructure which is hard to be distinguished from average structure in BNT ceramic [13]. The 0≤*x*≤0.15 samples are identified to be the AFE$_O$ P phase with a *Pbma* space group. With increasing BNT content up to *x*=0.18, the phase structure changes to the AFE$_O$ R phase with a *Pnma* space group [22,35]. The coexistence of AFE$_O$ P and R phases can be identified in the compositions of 0.16≤*x*<0.18. When the BNT content reaches up to *x*=0.35, a paraelectric (PE) orthorhombic (PE$_O$) T$_1$ phase with *Ccmm* space group can be identified at room temperature. With further increasing *x* up to 0.4, the high temperature PE tetragonal (PE$_T$) T$_2$ phase with *P4/mbm* was shifted to room temperature. As BNT content increases to *x*=0.5, a mixed phase
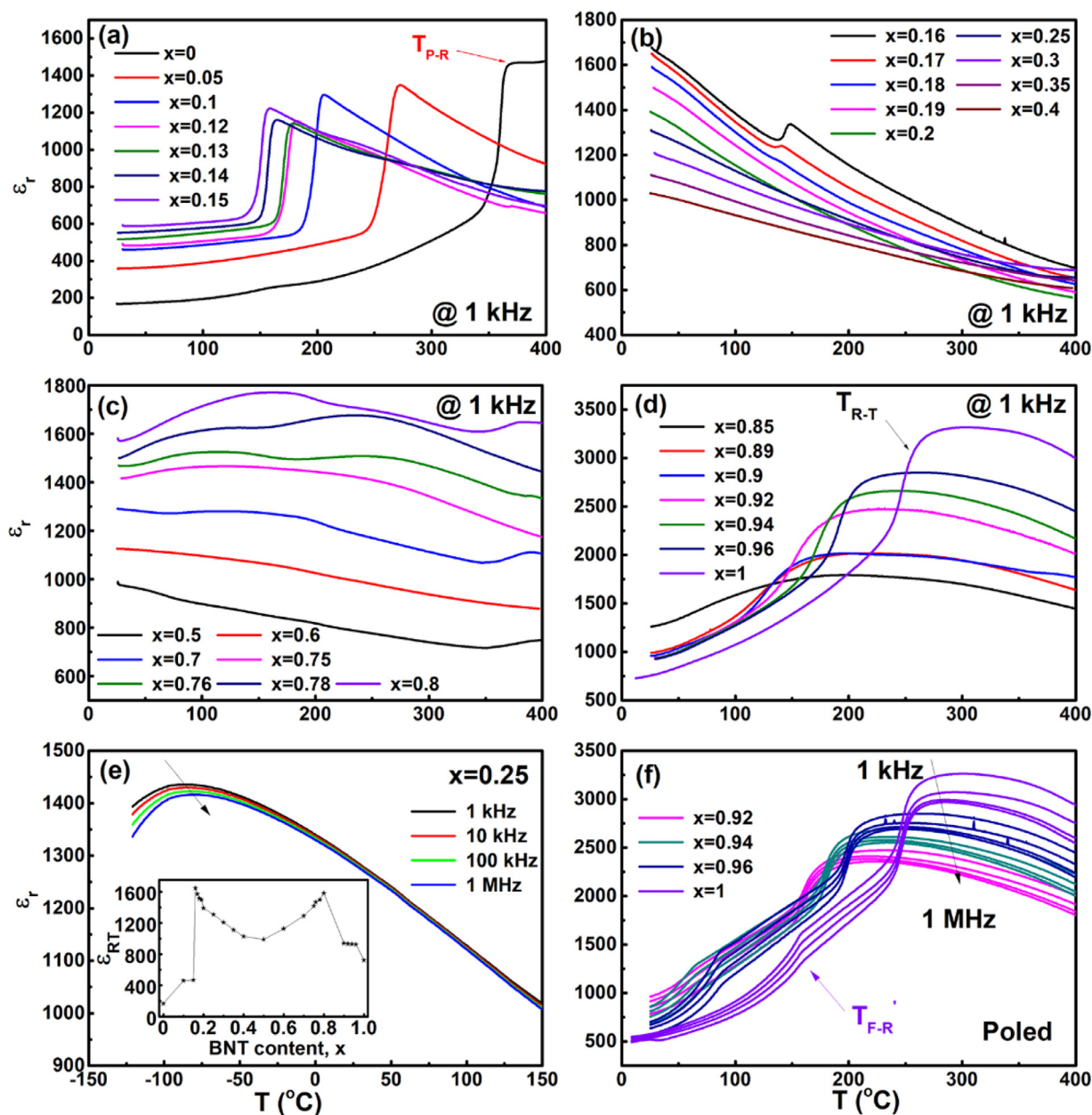
Fig. 4. (a)-(d) The dielectric permittivity as a function of temperature at a fixed frequency of 1 kHz for (1-x)NN-xBNT ceramics; The dielectric permittivity as a function of temperature and frequency for (e) virgin x=0.25 and (f) poled (1-x)NN-xBNT ceramics. The inset of (e) is the evolution of room-temperature dielectric permittivity at 1 kHz with changing BNT content.

including 48% P4/mbm and 52% P4bm can be identified. This P4bm phase should originate from the high temperature relaxor AFE phase in pure BNT. As 0.6≤x≤0.78, the phase structure gradually transforms into a P4bm phase. An FE rhombohedral (FE$_R$) phase with R3c space group, which should inherit from the low-temperature phase of BNT, can be achieved in the composition range of 0.85≤x≤1. A phase boundary between P4bm and R3c can be found approximately in the composition range of 0.78<x<0.85.

Fig. 6a shows Raman spectra for (1-x)NN-xBNT ceramics at room temperature to further confirm the phase structure of the studied samples, because Raman spectroscopy can probe a local ionic configuration within short-length scale [25,32,36]. The spectral deconvolution was performed using Gaussian-Lorentzian function. According to the fitting results, the wave number of several selected Raman peaks was plotted as a function of BNT content, as shown in Fig. 6b. The vibrations observed in Fig. 6a can be separated into translational modes of the isolated A site cations (Bi^{3+} and Na$^+$ in the low wave number range of <150 cm^{-1}) and internal modes of the coordination octahedra ($v1$, $v2$, $v3$, $v4$, $v5$, and $v6$). In these modes, $v1$–$v3$ are stretching modes and $v4$–$v6$ are bending modes [37]. Multi-peak Raman spectra below 300 cm^{-1} can be obviously seen for the NN ceramic, which are characteristic of the AFE P phase based on large difference between Nb-O bond lengths induced by the antiparallel off-centering displacement of Nb. With increasing BNT content, the rise and fall of the Raman spectra below 300 cm^{-1} become mild, although Raman peaks shift to lower wavenumbers. A drastic increase in the frequency for the Raman peaks around 175 cm^{-1}, 250 cm^{-1} and 600 cm^{-1} can be found as x=0.16, even though the amount of Raman peaks does not change. This should be related to the phase transition from the AFE$_O$ Pbma (P phase) to the AFE$_O$ Pnma (R phase), accompanying
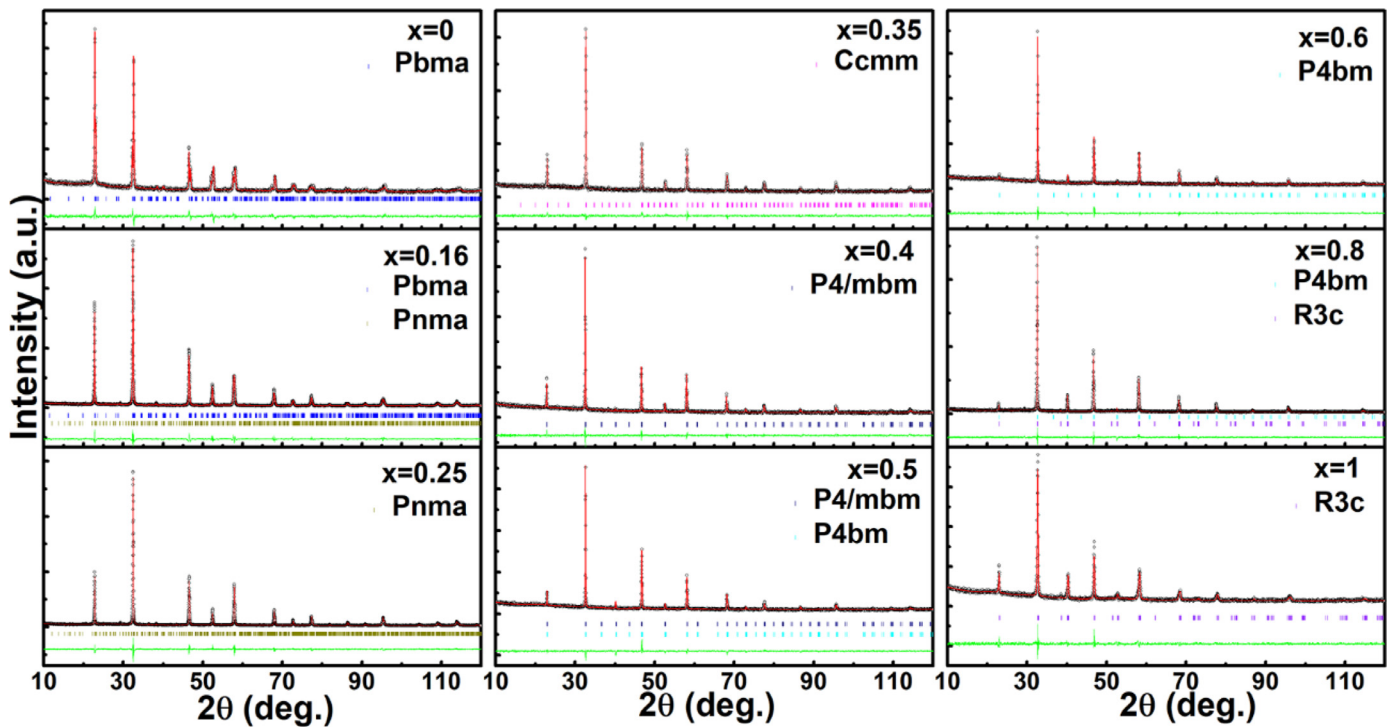
Fig. 5. Rietveld refinement plots of a few selected (1-x)NN-xBNT ceramics.

Table 1
Refined structural parameters by using the Rietveld method for (1-x)NN-xBNT ceramics measured at room temperature.

x	Space group	Lattice parameters	V (Å³)	R_{wp} (%)	R_p (%)	χ^2
0	Pbma	a=5.5631(2) Å, b= 15.5477(6) Å, c=5.4946(2) Å, α=β=γ=90°	475.170(48)	6.68	5.27	1.96
0.05	Pbma	a=5.5508(2) Å, b=15.5454(6) Å, c=5.4956(2) Å, α=β=γ=90°	474.204(47)	6.77	5.31	1.71
0.1	Pbma	a=5.5443(2) Å, b=15.5460(7) Å, c=5.4990(2) Å, α=β=γ=90°	473.979(50)	7.18	5.57	1.54
0.15	Pbma	a=5.5396(2) Å, b=15.5462(7) Å, c=5.5023(2) Å, α=β=γ=90°	473.866(48)	7.81	6.03	1.46
0.16	Pbma (16%)	a=5.5376(2) Å, b=15.5444(6) Å, c=5.5035(1) Å, α=β=γ=90°	473.754(44)	7.58	5.54	1.71
	Pnma (84%)	a=7.7884(5) Å, b=7.7900(4) Å, c=23.3739(8) Å, α=β=γ=90°	1418.153(86)			
0.18	Pnma	a=7.7802(5) Å, b=7.7883(6) Å, c=23.3949(9) Å, α=β=γ=90°	1417.613(96)	7.21	5.42	1.42
0.2	Pnma	a=7.7938(2) Å, b=7.7892(3) Å, c=23.3501(8) Å, α=β=γ=90°	1417.536(82)	7.45	5.79	1.80
0.25	Pnma	a=7.7931(2) Å, b=7.7888(3) Å, c=23.3461(7) Å, α=β=γ=90°	1417.100(80)	7.11	5.56	1.74
0.3	Pnma	a=7.7927(3) Å, b=7.7887(3) Å, c=23.3473(8) Å, α=β=γ=90°	1416.804(88)	7.33	5.66	1.76
0.35	Ccmm	a=7.7866(4) Å, b=7.7832(6) Å, c=7.7885(5) Å, α=β=γ=90°	472.015(48)	7.49	5.88	1.68
0.4	P4/mbm	a=b=5.5013(1) Å, c=3.8959(1) Å, α=β=γ=90°	117.913(8)	7.74	6.07	1.64
0.5	P4/mbm (48%)	a=b=5.5009(4) Å, c=3.8955(6) Å, α=β=γ=90°	117.888(17)	8.16	6.09	1.91
	P4bm (52%)	a=b=5.4993(1) Å, c=3.8964(1) Å, α=β=γ=90°	117.839(9)			
0.6	P4bm	a=b=5.4987(1) Å, c=3.8946(1) Å, α=β=γ=90°	117.795(8)	8.21	6.30	1.82
0.7	P4bm	a=b=5.4990(1) Å, c=3.8939(1) Å, α=β=γ=90°	117.749(9)	7.86	6.16	1.65
0.78	P4bm	a=b=5.4989(1) Å, c=3.8938(1) Å, α=β=γ=90°	117.744(9)	7.03	5.12	1.25
0.8	P4bm (69%)	a=b=5.5019(1) Å, c=3.8891(1) Å, α=β=γ=90°	117.728(7)	7.22	5.85	1.31
	R3c (31%)	a=b=5.4981(1) Å, c=13.4776(5) Å, α=γ=90°, β=120°	352.846(15)			
0.85	R3c	a=b=5.4980(4) Å, c=13.4754(9) Å, α=γ=90°, β=120°	352.512(16)	7.80	6.02	1.47
0.9	R3c	a=b=5.4907(2) Å, c=13.4778(6) Å, α=γ=90°, β=120°	351.894(35)	8.15	6.39	1.49
1	R3c	a=b=5.4830(4) Å, c=13.5073(9) Å, α=γ=90°, β=120°	351.683(46)	8.18	6.37	1.51

the decrease of the difference between B-O bond lengths in each oxygen octahedron [20]. An obvious broadening of the Raman bands centered at about 250 cm^{-1} and 600 cm^{-1} at x≥0.2 can be ascribed to the appearance of obvious dielectric relaxation behavior. Further broadening of Raman peaks as well as the emergence of Raman peaks at ~230 cm^{-1} at x=0.35 indicates the entrance into the PE phase zone with Ccmm space group. The splitting of the Ti/Nb-O modes (υ5 and υ4) can be observed in the composition range of 0.4≤x≤0.8, suggesting the tetragonal feature of the unit cell [38]. This is because the υ4 mode represents the double-degenerate O-B-O stretching vibration in which oxygen is situated along the c-axis, however, the υ5 mode corresponds to the triple-degenerate O-B-O bending vibration where the oxygen is located at

the ab plane perpendicular to the c-axis. The high-frequency Nb-O stretching bands around 600 cm^{-1} and the υ5 bending mode tend to shift to lower frequencies with increasing BNT content, indicating that the Nb/Ti-O vibrations become softened gradually as a result of weakening of the bonding between B-site cations and oxygen. The weakening of B-O bonds is compatible with the appearance of the dielectric relaxation behavior since the loss of hybridization between the empty Nb^{5+}/Ti^{4+} d-orbitals and the oxygen p-orbitals is closely related to the dielectric relaxation behavior [39]. The hardening behavior of Nb/Ti-O vibrations can be reflected by the increased wavenumbers of υ4-υ6 modes as x≥0.5 owing to the appearance of antipolar nanoregions (APNRs) [31] accompanied by the transformation from PE$_T$ P4/mbm to relaxor AFE$_T$ P4bm
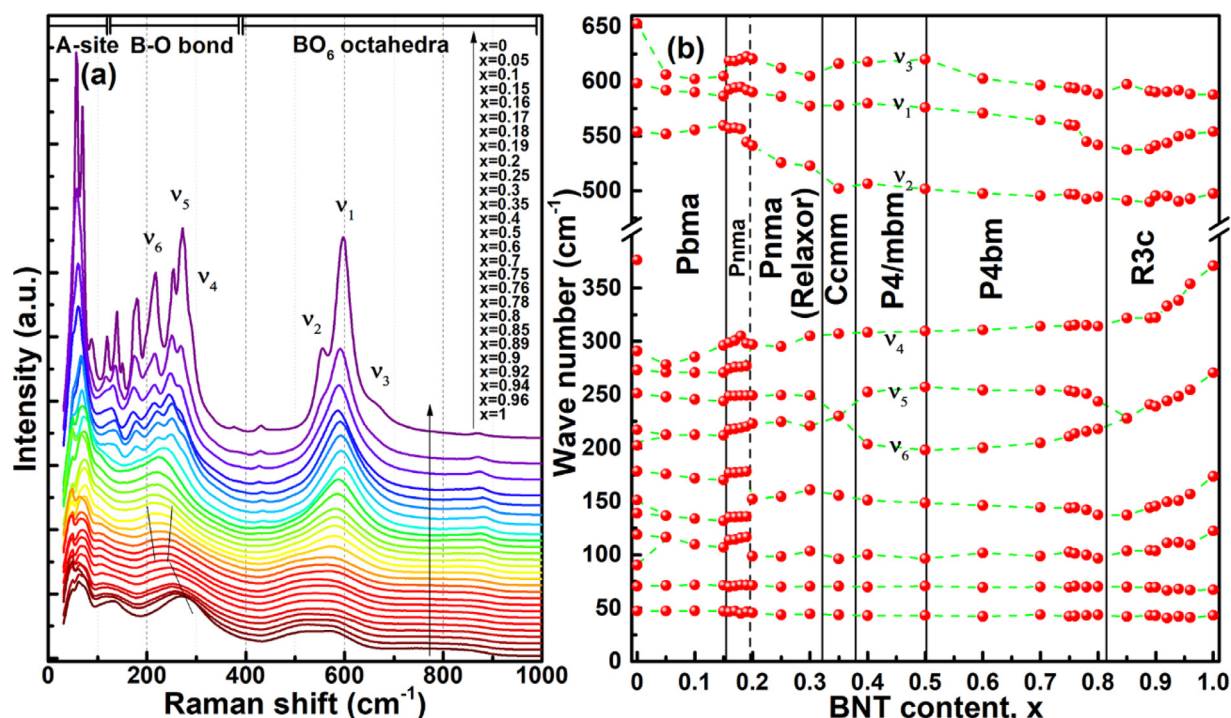
Fig. 6. (a) Raman spectra for (1-x)NN-xBNT ceramics at room temperature; (b) composition dependence of the wave number of several selected Raman peaks as determined by the multiple peak fitting of *Gauss-Lorentzian* function to the spectra.

Table 2

Phase structure information and the superlattice reflections achieved from SAED for the (1-x)NN-xBNT ceramics. (b*=AACC and c*=A0CA0C)[32]

x	Space group	Symmetry	Z	Pseudocubic cell	Tilt system	Superlattice (in SAED)
0–0.15	*Pbma*	Orthorhombic (AFE)	8	$\sqrt{2}a_P \times 4b_P \times \sqrt{2}a_P$	$a^-b^*a^-$	(2h,k,2l)/4
0.16–0.3	*Pnma*	Orthorhombic (AFE)	24	$2a_P \times 2b_P \times 6c_P$	$a^+b^-c^*$	(3h,3k,l)/6
0.35	*Ccmm*	Orthorhombic (PE)	8	$2a_P \times 2b_P \times 2c_P$	$a^-b^\circ c^+$	(h,2k,2l+1)/2
0.4–0.5	*P4/mbm*	Tetragonal (PE)	2	$\sqrt{2}a_P \times \sqrt{2}a_P \times c_P$	$a^0a^0c^+$	(2h+1,2k+1,2l)/2
0.5–0.8	*P4bm*	Tetragonal (relaxor-AFE)	2	$\sqrt{2}a_P \times \sqrt{2}a_P \times c_P$	$a^0a^0c^+$	(2h+1,2k+1,2l)/2
0.8–1	*R3c*	Rhombohedral (relaxor-FE)	6	$\sqrt{2}a_P \times \sqrt{2}a_P \times 3c_P$	$a^-a^-a^-$	(2h+1,2k+1,2l+1)/2

at x=0.5. The $\upsilon 4$ and $\upsilon 5$ merge together at x=0.85, further indicating the entrance into the FE$_R$ *R3c* phase zone. In addition, the Raman peaks around 150 cm^{-1}, 250 cm^{-1} and 600 cm^{-1} shift to higher frequencies in the *R3c* phase zone with increasing x, suggesting the hardening of B-O vibrations owing to the weakening of dielectric relaxation degree.

3.4. Analysis of domains

In order to clearly show the tilting system of some AFEs with long period modulated phases, such as *Pbma* ($\sqrt{2} \times 4 \times \sqrt{2}$) and *Pnma* ($2 \times 2 \times 6$) space groups shown in Fig. 1a, a new special notation that describes the tilts in terms of clockwise (C), anticlockwise (A) and zero (0) of adjacent octahedra was given by *Peel et al.* in order to improve the Glazer notation which is applicable to only $2 \times 2 \times 2$ supercell of the basic perovskite unit cell [29,35]. Owing to the distinction of the crystal symmetry as well as the tilting system in different phases, obvious differences can be found on bright-field TEM images and the corresponding SAED patterns, as displayed in Fig. 7 for several typical (1-x)NN-xBNT compositions. The phase structure information as well as the superlattice reflections achieved from SAED in Fig. 7 are summarized in Table 2. For the x=0.1 ceramic, the polydomain morphology being composed of micrometer-sized domain blocks was manifested in Fig. 7a. The AFE feature with *Pbma* space group can be further identified by the quarter integer superlattice diffraction spots obtained from the

SAED pattern owing to the existence of *AACC* tilting along *b* axis. For the AFE$_O$ R phase with *Pnma* space group in the x=0.18 sample, stripe domains of tens of nanometers in width were observed, as shown in Fig. 7c. The most possible structure model for the *Pnma* phase in NN is given as $a^-b^+c^*$ (c*=A0CA0C, see Fig. 1a), thus *(3h,3k,l)/6* superlattice reflections can be observed, as shown in Fig. 7c1. As shown in Fig. 7b, stripe domains with inhomogeneous width as well as superlattice lines instead of superlattice spots can be found in x=0.16 ceramic as a result of the formation of the incommensurate phase caused by the coexistence but random distribution of P and R phases. Accompanying the appearance of obvious dielectric relaxation behavior at x≥0.2, stripe domains change to be randomly distributed APNRs, as shown in Fig. 7d. Yet, *1/6* typed superlattice spots can be still detected in x=0.25 ceramic, suggesting that the intrinsic structure of the APNRs is still the AFE$_O$ symmetry with *Pnma* space group [5]. Compared with the x=0.18 sample with a normal AFE phase, the x=0.25 sample exhibits weak and even partially unclear superlattice reflections, because the measuring zone (~100 nm in diameter and ~100 nm in thickness) for the SAED is much larger than the size of nanodomains. A smooth domain morphology with little contrast can be observed in the x=0.35 ceramic in Fig. 7e, just corresponding to the PE phase with no spontaneous polarization in perovskite unit cells. However, octahedra tilting still exists as $a^-b^\circ c^+$ (see Fig. 7e1), indicating that this PE phase is not a cubic phase but an orthorhombic phase with *Ccmm* space group. Therefore, the
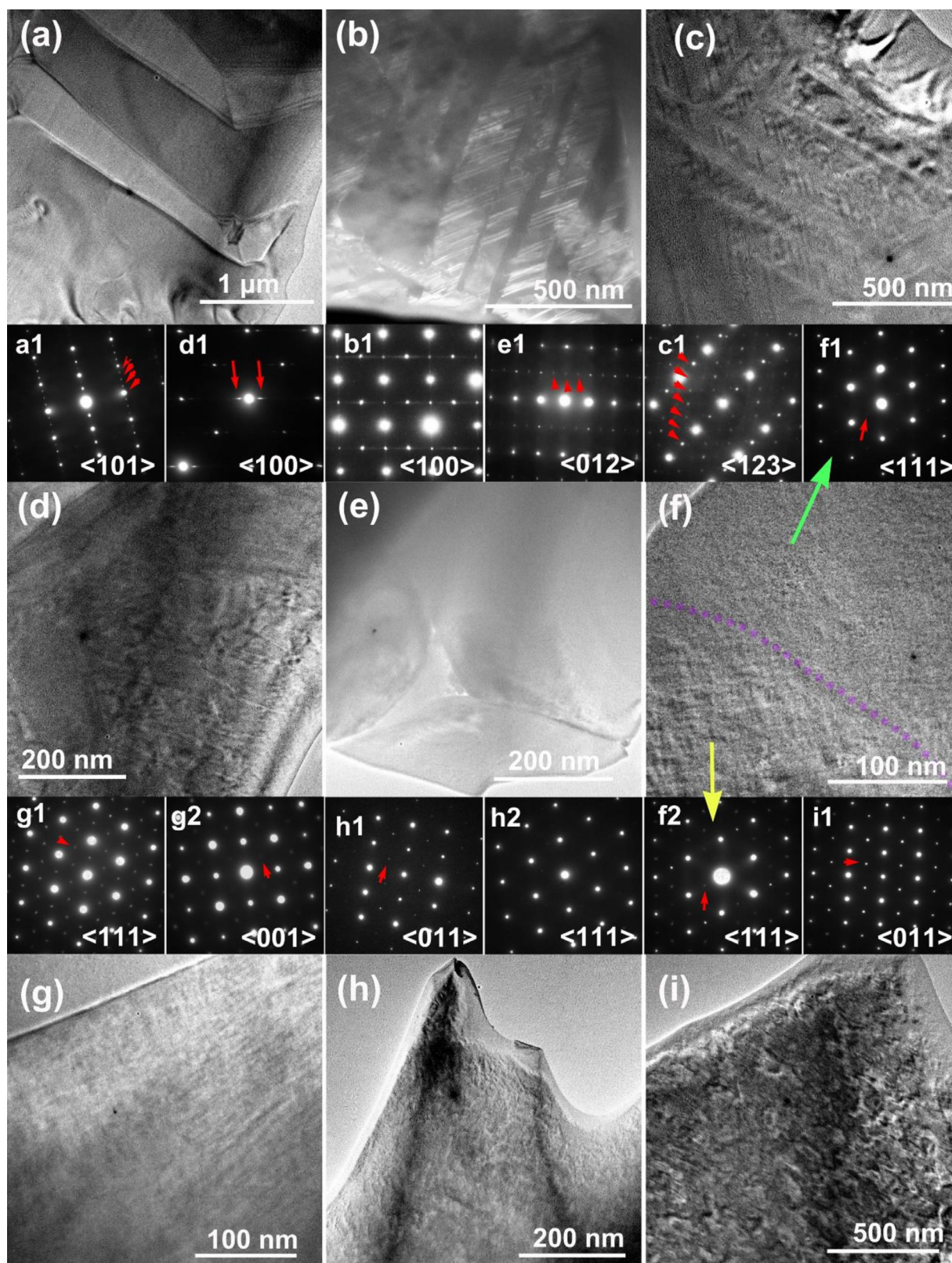
Fig. 7. Room temperature bright-field TEM image and the corresponding SAED patterns of (1-*x*)NN-*x*BNT ceramics with (a) *x*=0.1, (b) *x*=0.16, (c) *x*=0.18, (d) *x*=0.25, (e) *x*=0.35, (f) *x*=0.5, (g) *x*=0.78, (h) *x*=0.9 and (i) *x*=1.

characteristic half-integer superlattice spots as *(h,2k,2l+1)/2* can be observed along *[012]$_C$* direction. Both of *P4/mbm* and *P4bm* tetragonal phases exhibit $a^0a^0c^+$ octahedra tilting, resulting in typical *(2h+1,2k+1,2l)/2* superlattice reflections for the *x*=0.5 sample, as shown in Fig. 7f. However, the different thing is that *P4/mbm* be-

longs to a PE phase, while *P4bm* is an AFE phase with strong dielectric relaxation behavior [7,8]. Nanodomains with faint contrasts can be found at the lower-left corner of Fig. 7f. The other part of the grain exhibits little contrasts, further confirming the coexistence of two different tetragonal phase structures in the
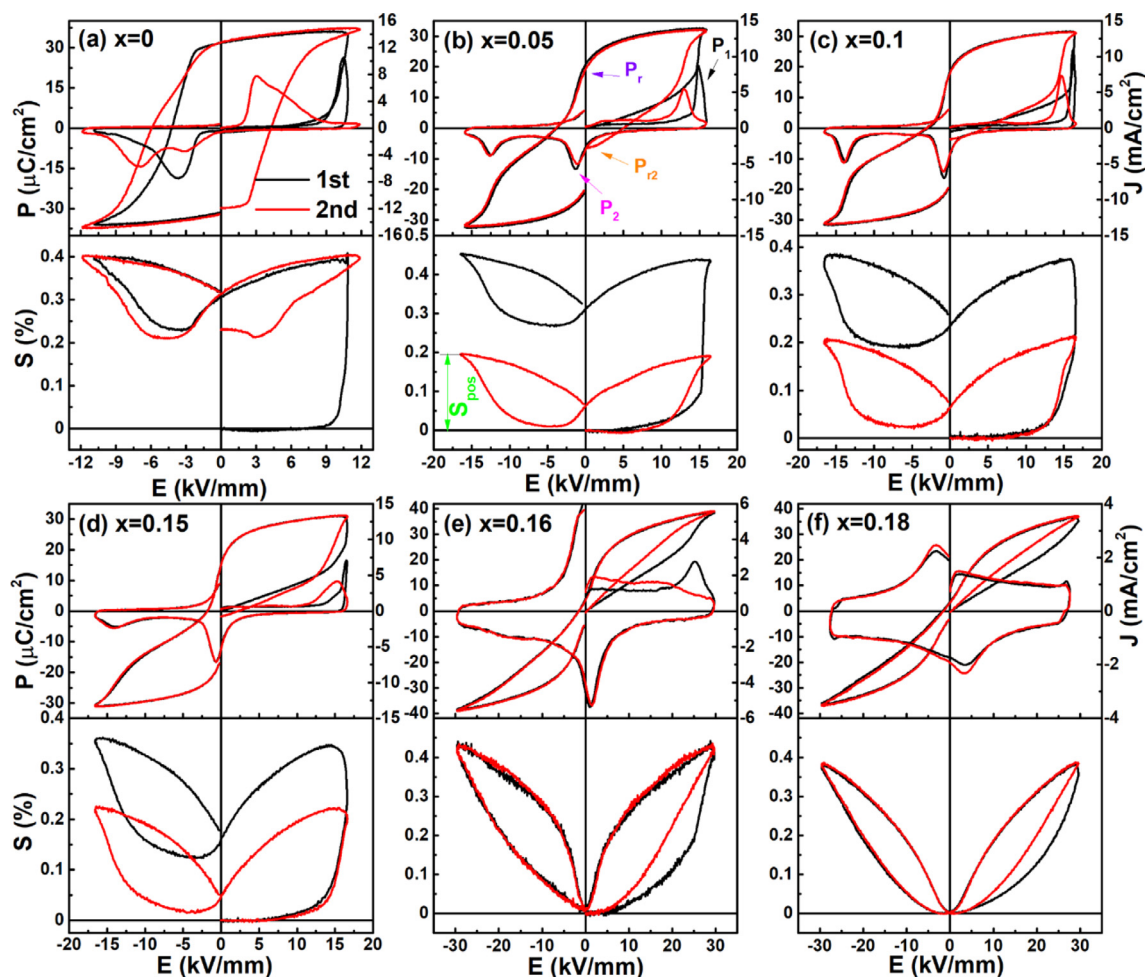
Fig. 8. *P-E, S-E* loops and the corresponding *J-E* curves at 10 Hz during the first and second electric cycles for (1-*x*)NN-*x*BNT ceramics: (a) *x*=0, (b) *x*=0.05, (c) *x*=0.1, (d) *x*=0.15 (e) *x*=0.16 and (f) *x*=0.18.

composition of *x*=0.5, as proved by Figs.7f1 and 7f2. Nanodomains with faint contrasts can be also observed in the *x*=0.78 and *x*=0.9 ceramics, belonging to the typical feature of ergodic (A)FEs, as shown in Figs. 7g and 7h, respectively. The tetragonal phase with *(2h+1,2k+1,2l)/2* superlattice diffraction spots (Figs. 7g1 and 7g2) and the rhombohedral phase with *(2h+1,2k+1,2l+1)/2* superlattice spots (Figs. 7h1 and 7h2) are detected in *x*=0.78 and *x*=0.9 ceramics, respectively, indicating that those two compositions at room temperature belong to the AFE *P4bm* and FE *R3c* phases, respectively. For pure BNT ceramic in Fig. 7i, irregular or dirty domain morphology together with *(2h+1,2k+1,2l+1)/2* superlattice reflections can be observed, suggesting an *R3c* FE phase.

3.5. Reversibility of field induced AFE-FE phase transition

Besides the AFE phase stability, the reversibility of the AFE-FE phase transition is also very important. Fig. 8 shows the polarization switching and strain behavior during the first and second electric cycles for AFE P and R compositions of 0≤*x*≤0.18. A sharp polarization current peak (P$_1$) can be observed in the NN ceramic during the first cycle as a result of the field induced AFE to FE phase transition. A nearly square *P-E* loop was obtained during the second cycle, suggesting that AFE NN irreversibly transforms into an FE phase after poling. However, as *x*≥0.05, typical double *P-E* hysteresis loops with two current peaks (P$_1$ and P$_2$ at E_{A-F} and E_{F-A} for the AFE-FE/FE-AFE phase transition, respectively) can be obtained during both first and second electric cy-

cles, further confirming the enhanced stability of the AFE phase. A small remanent polarization P_{r2} can be observed during the second electric cycle for the *x*=0.05 ceramic, indicating the existence of a small amount of FE phase after poling. However, reproducible double *P-E* loops with near-zero P_{r2} for the *x*≥0.1 compositions suggest that the substitution of BNT for NN tends to stabilize the AFE phase and enhance the reversibility of the AFE-FE phase transition. Moreover, as *x*≥0.16, not only *P-E* loops but also *S-E* curves can be well repeated during different electric field cycles. By comparison, the 0.1≤*x*≤0.15 compositions exhibit repeated *P-E* loops but irreproducible *S-E* curves, indicating that the electric field induced FE phase returns to a new AFE phase rather than its initial AFE$_O$ P phase after removal of external electric fields [28]. The difference in the crystal symmetry between the initial AFE$_O$ and the metastable poled AFE phase is believed to be responsible for the poling strain gap between the first cycle and non-first electric field cycles [28]. An obvious decrease of P_r values for compositions with AFE$_O$ R phase (*x*≥0.16) indicates a decreased polarization hysteresis during field induced AFE-FE phase transition, although both E_{A-F} and E_{F-A} values increase rapidly. More importantly, the field-induced AFE$_O$ R to FE phase transition should be completely reversible during different electric field cycles. A recoverable large strain ~0.44% can be generated in the *x*=0.16 sample, indicating a large application potential in large-strain actuators for NN-based lead-free AFE ceramics. Nevertheless, the driving electric field E_{A-F} of the AFE$_O$ R phase in this study is higher than that for NaNbO$_3$-SrTiO$_3$ (NN-ST) binary system [33].
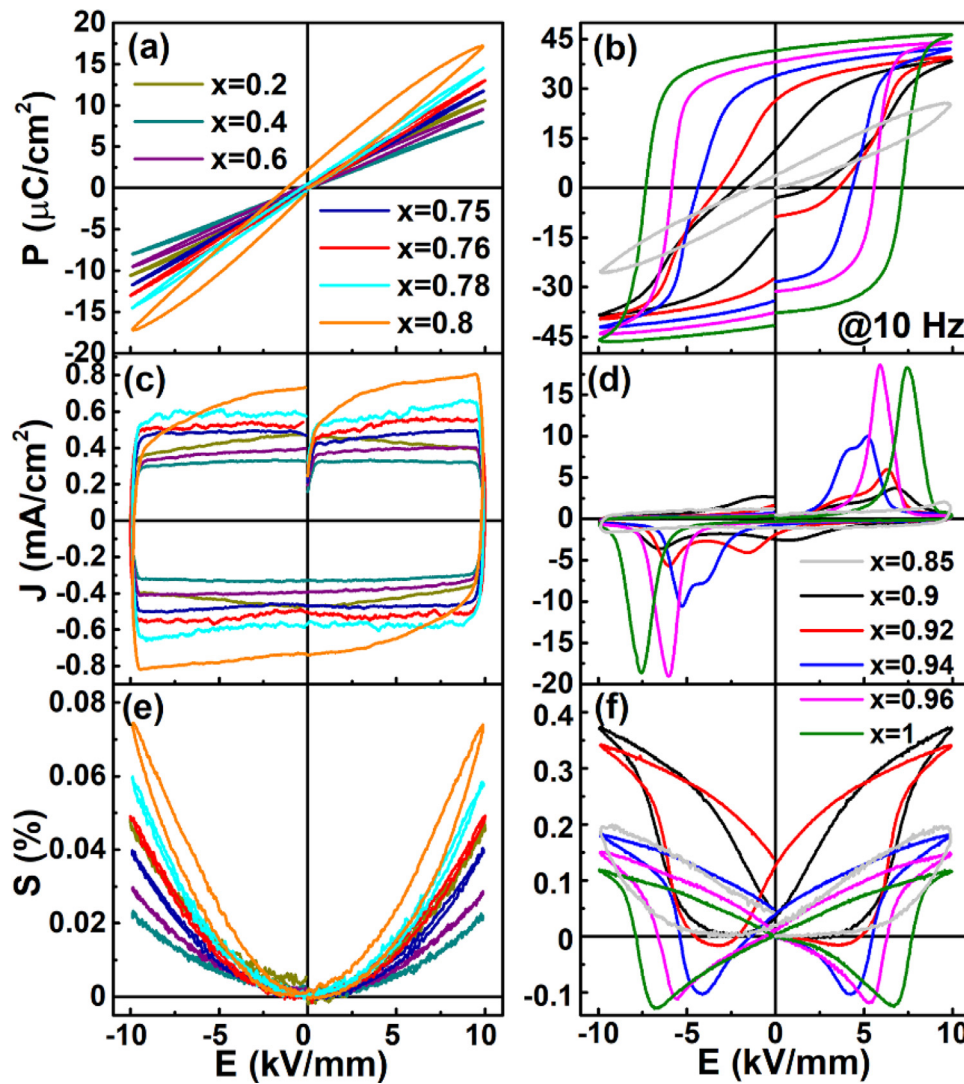
Fig. 9. (a),(b) Room-temperature *P-E* hysteresis loops, (c),(d) the corresponding *J-E* curves and (e),(f) bipolar *S-E* curves for (1-*x*)NN-*x*BNT ceramics.

Fig. 9 shows *P-E* hysteresis loops, the corresponding *J-E* curves and bipolar *S-E* curves measured at room temperature for the (1-*x*)NN-*x*BNT ceramics with *x*>0.18. Owing to existence of large random field manifested by strong dielectric relaxation behavior, a large E_{A-F} is needed to drive the AFE-FE phase transition for relaxor AFE compositions. As a result, nearly linearly P-E response and parabolic S-E response can be found in the studied electric field range for the PE (0.35<*x*<0.5) and relaxor AFE phase zones (0.2≤*x*≤0.35 and 0.5≤*x*≤0.8. Pinched *P-E* loop and significantly enhanced electrostrain (~0.38%) at *x*=0.9 further indicate that this composition should be located at the phase boundary between ergodic and nonergodic relaxor FEs.

4. Discussion

4.1. Phase diagram of NN-BNT binary system

Based on the above discussion, the phase diagram of (1-*x*)NN-*x*BNT binary system was plotted, as shown in Fig. 10. It can be clearly found that the formation of solid solution tends to shift the polymorphic phase transition temperatures of end members, both NN and BNT, to lower temperatures, resulting in the complex phase change with changing composition. Besides, obvious change of dielectric relaxation behavior can be also detected. The T_{F-R}'

(~T_f) can be used to reveal the nonergodic to ergodic phase transition, even though there might be no change in the local symmetry. Differently, no phase structure generally changes at the temperature of dielectric maxima (T_m). As a consequence, an unstable AFE$_O$ *Pbma* phase, a partially stable AFE$_O$ *Pbma* phase, a completely stable AFE$_O$ *Pnma* phase, a PE$_O$ *Ccmm* phase, a PE$_T$ *P4/mbm* phase, a relaxor AFE$_T$ *P4bm* phase, an ergodic relaxor FE$_R$ *R3c* phase and finally a nonergodic relaxor FE$_R$ *R3c* phase sequentially appear at room temperature in (1-*x*)NN-*x*BNT solid solution with increasing BNT content. In the proximity of *x*=0.5, although there are two kinds of tetragonal phases, one belongs to the PE phase (*x*<0.5) and the other belongs to the AFE phase (*x*>0.5). Multiple AFE phases of different crystal symmetries and varying stability can be induced by changing BNT content, resulting in various types of phase boundaries. It can be found that the phase diagram was constructed mainly according to the qualitative analysis about the symmetry change caused by octahedral tilting system change. Cation off-centering displacement should be another important factor affecting polarization properties and symmetry in AFEs/FEs, especially during the process of AFE-FE phase transition [19] which is rarely involved in this binary system. Therefore, some details might be not elaborate enough in the phase diagram, such as the disappearance of ferroelectricity in NN after adding BNT. Even so, a significant phase diagram can be achieved owing to
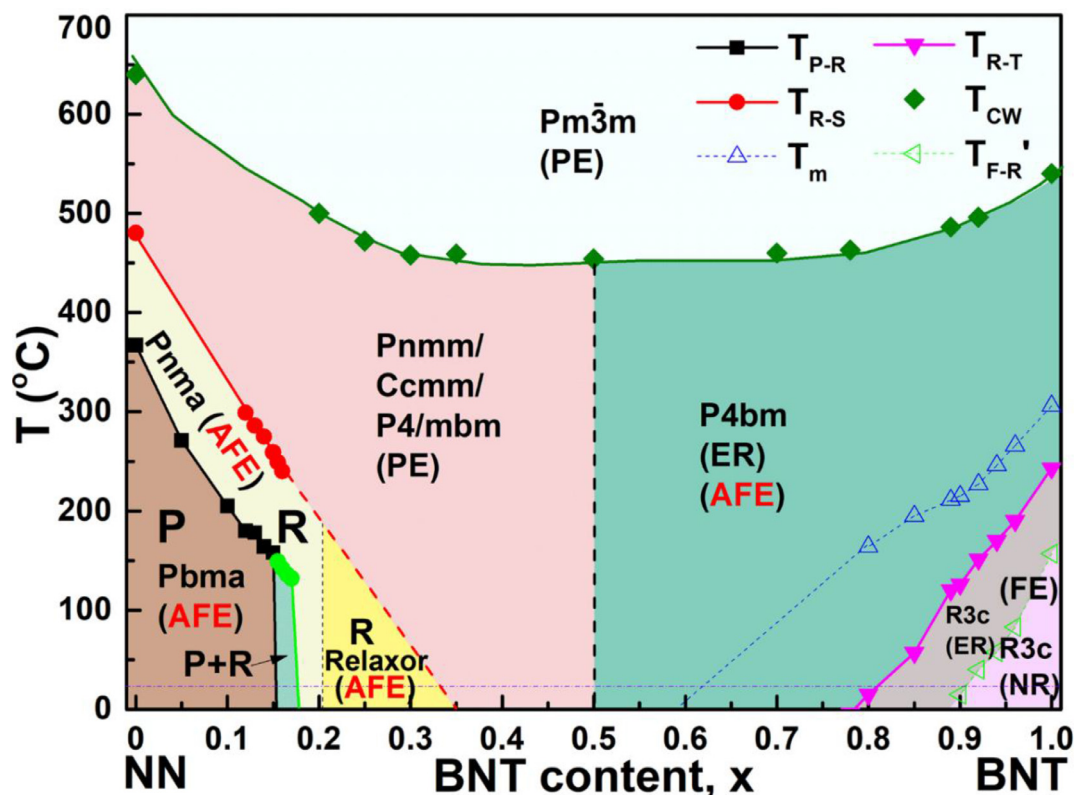
Fig. 10. Phase diagram of (1-*x*)NN-*x*BNT binary system plotted based on results of dielectric, ferroelectric, XRD, Raman and TEM measurements (ER: Ergodic, NR: Nonergodic; T_{R-S} corresponds to the phase transition temperature from the AFE R *Pnma* to the PE S *Pnmm*; T_{CW} stands for the *Curie-Weiss* temperature).

the complex change of octahedral tilting. Further quantitative local structure information would be studied in future by using higher resolution methods [19].

4.2. Metastable monoclinic AFE and tetragonal (P4bm) AFE phases

In order to further clarify the structure mechanism for the reversibility of AFE-FE phase transition in response to external electric fields for (1-*x*)NN-*x*BNT compositions with different AFE phases, *in-situ* synchrotron XRD results of three representative compositions with $x=0.05$ (AFE$_O$ P phase), $x=0.1$ (AFE$_O$ P phase) and $x=0.18$ (AFE$_O$ R phase) are shown in Fig. S1. A typical $(110)_C$ triplet and a $(200)_C$ doublet corresponding to an orthorhombic phase can be observed in all three studied virgin samples. When a strong external field is applied (17 kV/mm for the $x=0.05$ and 0.1 samples, 30 kV/mm for the $x=0.18$ sample), new reflections corresponding to a monoclinic symmetry can be detected in both $(110)_C$ and $(200)_C$ diffraction peaks, indicating that both AFE$_O$ P and AFE$_O$ R phases can be forced into an FE monoclinic (FE$_M$) phase under high fields. After removal of external electric field, an AFE monoclinic (AFE$_M$) dominated phase can be observed in the poled $x=0.05$ and $x=0.1$ samples (see Fig. S1a and S1b), meaning that the AFE$_O$-FE$_M$ phase transition is incompletely reversible. By comparison, an AFE$_O$ phase can be found in the poled $x=0.18$ sample (Fig. S1c), further confirming that the AFE$_O$ R phase is stable enough to show a completely reversible field induced AFE$_O$-FE$_M$ phase transition. The reversibility of AFE-FE phase transition can be further confirmed by the Rietveld refinement on full profiles of XRD patterns of poled (1-*x*)NN-*x*BNT ceramic powders shown in Fig. S1 and Table S1. The results indicate that the poled NN ceramic should belong to an FE$_M$ *Pm* phase at room temperature. Moreover, it can be seen that the overall fit between the observed and calculated profiles for the poled $x=0.05$ ceramic powder is very good based on the coexistence of AFE$_M$ *P2$_1$* and FE$_M$ *Pm* phases. The existence

of a small amount of FE$_M$ phases in the poled sample means that the AFE phase in the $x=0.05$ sample is not stable enough. With increasing BNT content, a pure AFE$_M$ *P2$_1$* ($\sqrt{2}a_P \times 4b_P \times \sqrt{2}c_P$) can be identified for the poled $x=0.1$ and $x=0.15$ samples, which exhibits the same octahedral tilt system of $a^- b^* c^-$ ($b^* = AACC$) to that of AFE P *Pbma* phase, as shown in the inset of Fig. S1b. By comparison, the poled $x=0.18$ sample can be identified to be the AFE$_O$ R phase with a *Pnma* space group, further confirming a completely reversible AFE-FE phase transition. These phenomena are similar to those observed in NN-ST samples where a metastable AFE$_M$ phase ($P2_1$) exists after removal of high external electric fields for the AFE P phase composition [33].

The reversible field forced phase transition can also be found in BNT-rich compositions in the proximity of the ergodic-nonergodic relaxor ($x\sim0.9$) and AFE-FE ($x\sim0.8$) phase boundaries. Owing to the existence of large random field, a relatively high electric field should be needed for driving the relaxor AFE to FE phase transition. Compared with the composition close to the ergodic-nonergodic relaxor phase boundary, the ceramic close to the AFE-FE phase boundary exhibits relatively small electrostrains in BNT-rich compositions (see Fig. 9). However, fast *P-E* and *S-E* response of these APNRs provides the structural foundation for generating excellent electrostrictive and energy storage properties in AFE$_T$ *P4bm* ceramics [9,31].

4.3. Outstanding electrical performances

Fig. S2 shows several representative electrical properties of (1-*x*)NN-*x*BNT lead-free ceramics. Accompanying the appearance of multiple AFE phases with different stability and dielectric relaxation behavior, the room temperature dielectric permittivity thus exhibits a complex dependence of composition. Large dielectric permittivity of ~1500 with an ultra-high temperature limit value $T_{\pm10\%}$ (>350 °C), which stands for the upper-limit temperature for

the permittivity variation within $\pm 10\%$ of the room-temperature permittivity, can be detected in the $x=0.78$ composition with an AFE$_T$ *P4bm* phase (see Fig. 4) [9], showing large advantages in thermally-stable ceramic capacitors. Excellent electrostrictive characteristics (low strain hysteresis) were reported in the relaxor AFEs ($x=0.2$-0.35 and 0.5-0.8) in both NN-rich or BNT-rich compositions [9,31]. Most importantly, large recoverable energy storage density (W_{rec}) of over 4 J/cm^3 as well as large energy storage efficiency η of $>80\%$ can be obtained in both relaxor AFE$_O$ R and AFE$_T$ *P4bm* phase zones (see Fig. S2a), being expected to be potential dielectric materials for energy-storage capacitors [5,40,41]. Large electrostrains of ~0.4% (S_{pos} as indicated in Fig. 8b) can be generated in the AFE$_O$ R dominated samples ($x=0.16$) and ergodic relaxor FE ceramics ($x=0.9$-0.92) (see Fig. S2b) [28,33]. All these results indicate giant potentials in multifunctional applications for NN-BNT lead-free binary ceramics.

5. Conclusions

A full phase diagram of $(1\text{-}x)$NN-xBNT binary system was constructed according to the measurement of dielectric, ferroelectric properties, average and local structures, the Rietveld refinement of XRD data and the analysis of domain morphology and so on. The variation of the relative content of NN and BNT in continuous solid solution tends to introduce the dielectric relaxation, adjust the oxygen octahedral tilting and alter the stability of AFE phases, generating various reversibility of the AFE-FE phase transition and particularly relaxor AFE compositions with fast and linear polarization response. The room-temperature structure of different compositions evolves as follows: an unstable AFE$_O$ *Pbma* P phase ($x=0$) $\rightarrow$ a partially stable AFE$_O$ *Pbma* P phase ($0<x\leq0.15$) $\rightarrow$ an AFE$_O$ *Pbma* P and AFE$_O$ *Pnma* R coexisted phase ($0.15<x<0.18$) $\rightarrow$ a normal AFE$_O$ *Pnma* R phase ($0.18\leq x<0.2$) $\rightarrow$ a relaxor AFE$_O$ *Pnma* R phase ($0.2\leq x\leq0.3$) $\rightarrow$ a PE$_O$ *Ccmm* phase ($0.3<x<0.4$) $\rightarrow$ a PE$_T$ *P4/mbm* phase ($0.4\leq x<0.5$) $\rightarrow$a PE$_T$ *P4/mbm* and relaxor AFE$_T$ *P4bm* coexisted phase ($x=0.5$) $\rightarrow$ a relaxor AFE$_T$ *P4bm* phase ($0.5<x<0.8$) $\rightarrow$ a relaxor AFE$_T$ *P4bm* and ergodic FE$_R$ *R3c* coexisted phase ($x=0.8$) $\rightarrow$an ergodic FE$_R$ *R3c* phase ($0.8<x\leq0.9$) $\rightarrow$ finally a nonergodic FE$_R$ *R3c* phase ($0.9<x\leq1$). Among these compositions, emerging multiple AFE phases with different symmetries, stability and domain scales include AFE$_O$, AFE$_T$ and AFE$_M$, exhibiting fascinating application potentials in thermally-stable capacitors, dielectric energy storage and large-strain ceramic actuators.

Declaration of Competing Interest

The authors declare that they have no known competing financial interests or personal relationships that could have appeared to influence the work reported in this paper.

Acknowledgements

Supplementary materials

Supplementary material associated with this article can be found, in the online version, at doi:10.1016/j.actamat.2021.116710.

References

[1] E. Sawaguchi, H. Maniwa, S. Hoshino, Antiferroelectric structure of lead zirconate, Phys. Rev. 83 (1951) 1078.

[2] X.L. Tan, C. Ma, J. Frederick, S. Beckman, K.G. Webber, The antiferroelectric↔ferroelectric phase transition in lead-containing and lead-free perovskite ceramics, J. Am. Ceram. Soc. 94 (2011) 4091–4107.

[3] A.S. Mischenko, Q. Zhang, J.F. Scott, R.W. Whatmore, N.D. Mathur, Giant electrocaloric effect in thin-film PbZr$_{0.95}$Ti$_{0.05}$O$_3$, Science 311 (2006) 1270–1271.

[4] W.Y. Pan, C.Q. Dam, Q.M. Zhang, L.E. Cross, Large displacement transducers based on electric field forced phase transitions in the tetragonal (Pb$_{0.97}$La$_{0.02}$)(Ti,Zr,Sn)O$_3$ family of ceramics, J. Appl. Phys. 66 (1989) 6014.

[5] H. Qi, R.Z. Zuo, A.W. Xie, A. Tian, J. Fu, Y. Zhang, S.J. Zhang, Ultrahigh energy storage density in NaNbO$_3$-based lead-free relaxor antiferroelectric ceramics with nanoscale domains, Adv. Funct. Mater. (2019) 1903877.

[6] C. Kittel, Theory of antiferroelectric crystals, Phys. Rev. 82 (1951) 729.

[7] C. Ma, X.L. Tan, E. Dul'kin, M. Roth, Domain structure-dielectric property relationship in lead-free (1-x)(Bi$_{1/2}$Na$_{1/2}$)TiO$_3$-xBaTiO$_3$ ceramics, J. Appl. Phys. 108 (2010) 104105.

[8] G.O. Jones, P.A. Thomas, Investigation of the structure and phase transitions in the novel A-site substituted distorted perovskite compound Na$_{0.5}$Bi$_{0.5}$TiO$_3$, Acta Cryst. B 58 (2002) 168–178.

[9] H. Qi, R.Z. Zuo, Linear-like lead-free relaxor antiferroelectric (Bi$_{0.5}$Na$_{0.5}$)TiO$_3$-NaNbO$_3$ with giant energy-storage density/efficiency and super stability against temperature and frequency, J. Mater. Chem. A 7 (2019) 3971–3978.

[10] J.L. Li, F. Li, Z. Xu, S.J. Zhang, Multilayer lead-free ceramic capacitors with ultrahigh energy density and efficiency, Adv. Mater. (2018) 1802155.

[11] Y.P. Guo, M.Y. Gu, H.S. Luo, Y. Liu, R.L. Withers, Composition-induced antiferroelectric phase and giant strain in lead-free (Na$_y$,Bi$_z$)Ti$_{1-x}$O$_{3(1-x)}$-xBaTiO3 ceramics, Phys. Rev. B 83 (2011) 054118.

[12] Y.P. Guo, Y. Liu, R.L. Withers, F. Brink, H. Chen, Large electric field-induced strain and antiferroelectric behavior in (1-x)(Na$_{0.5}$Bi$_{0.5}$)TiO$_3$-xBaTiO$_3$ ceramics, Chem. Mater. 23 (2011) 219–228.

[13] Y. Liu, L. Norén, A.J. Studer, R.L. Withers, Y.P. Guo, Y.X. Li, H. Yang, J. Wang, Response of intergrown microstructure to an electric field and its consequences in the lead-free piezoelectric bismuth sodium titanate, J. Solid State Chem. 187 (2012) 309–315.

[14] A. Kania, J. Kwapulinski, Ag$_{1-x}$Na$_x$NbO$_3$ (ANN) solid solutions: from disordered antiferroelectric AgNbO$_3$ to normal antiferroelectric NaNbO$_3$, J. Phys.: Condens. Matter 11 (1999) 8933–8946.

[15] H. Shimizu, H.Z. Guo, S.E. Reyes-Lillo, Y. Mizuno, K.M. Rabe, C.A. Randall, Lead-free antiferroelectric: xCaZrO$_3$-(1-x)NaNbO$_3$ system (0<x≤0.10), Dalton Trans. 44 (2015) 10763–10772.

[16] Y. Tian, L. Jin, H.F. Zhang, Z. Xu, X.Y. Wei, E.D. Politova, S. Yu. Stefanovich, N.V. Tarakina, I. Abrahams, H.X. Yan, High energy density in silver niobate ceramics, J. Mater. Chem. A 4 (2016) 17279–17287.

[17] D. Fu, M. Endo, H. Taniguchi, T. Taniyama, M. Itoh, AgNbO$_3$: A lead-free material with large polarization and electromechanical response, Appl. Phys. Lett. 90 (2007) 252907.

[18] M. Yashima, S. Matsuyama, R. Sano, M. Itoh, K. Tsuda, D. Fu, Structure of ferroelectric silver niobate AgNbO$_3$, Chem. Mater 23 (2011) 1643–1645.

[19] T. Lu, Y. Tian, A. Studer, N. Narayanan, Q. Li, R. Withers, L. Jin, Y. Mendez–González, A. Peláiz-Barranco, D.H. Yu, G.J. McIntyre, Z. Xu, X.Y. Wei, H.X. Yan, Y. Liu, Symmetry-mode analysis for intuitive observation of structure-property relationships in the lead-free antiferroelectric (1-x)AgNbO$_3$-xLiTaO$_3$, IUCrJ 6 (2019) 740–750.

[20] A.C. Sakowski-Cowley, K. Łukaszewicz, H.D. Megaw, The structure of sodium niobate at room temperature, and the problem of reliability in pseudosymmetric structures, Acta Crystallogr. B 25 (1969) 851–865.

[21] S.K. Mishra, N. Choudhury, S.L. Chaplot, P.S.R. Krishna, R. Mittal, Competing antiferroelectric and ferroelectric interactions in NaNbO$_3$: Neutron diffraction and theoretical studies, Phys. Rev. B 76 (2007) 024110.

[22] S.K. Mishra, R. Mittal, V. Yu. Pomjakushin, S.L. Chaplot, Phase stability and structural temperature dependence in sodium niobate: A high-resolution powder neutron diffraction study, Phys. Rev. B 83 (2011) 134105.

[23] L.E. Cross, Electric double hysteresis in (K$_x$Na$_{1-x}$)NbO$_3$ single crystals, Nature 181 (1958) 178–179.

[24] L.M. Chao, Y.D. Hou, M.P. Zheng, M.K. Zhu, High dense structure boosts stability of antiferroelectric phase of NaNbO$_3$ polycrystalline ceramics, Appl. Phys. Lett. 108 (2016) 212902.

[25] R.A. Shakhovoy, S.I. Raevskaya, L.A. Shakhovaya, D.V. Suzdalev, I.P. Raevski, Yu.I. Yuzyuk, A.F. Semenchev, M.El Marssi, Ferroelectric Q and antiferroelectric P phases' coexistence and local phase transitions in oxygen-deficient NaNbO$_3$ single crystal: micro-Raman, dielectric and dilatometric studies, J. Raman Spectrosc. 43 (2012) 1141–1145.

[26] J.M. Ye, G.S. Wang, X.F. Chen, F. Cao, X.L. Dong, Enhanced antiferroelectricity and double hysteresis loop observed in lead-free (1-x)NaNbO$_3$-xCaSnO$_3$ ceramics, Appl. Phys. Lett. 114 (2019) 122901.

[27] L.S. Gao, H.Z. Guo, S.J. Zhang, C.A. Randall, Stabilized antiferroelectricity in xBiScO$_3$-(1-x)NaNbO$_3$ lead-free ceramics with established double hysteresis loops, Appl. Phys. Lett. 112 (2018) 092905.

[28] R.Z. Zuo, J. Fu, H. Qi, Stable antiferroelectricity with incompletely reversible phase transition and low volume-strain contribution in BaZrO$_3$ and CaZrO$_3$ substituted NaNbO$_3$ ceramics, Acta Mater 161 (2018) 352–359.

[29] A.M. Glazer, The classification of tilted octahedra in perovskites, Acta Cryst. B 28 (1972) 3384–3392.

[30] L. Li, M.K. Zhu, Q.M. Wei, M.P. Zheng, Y.D. Hou, J.G. Hao, Ferroelectric P4mm to relaxor P4bm transition and temperature-insensitive large strains in Bi(Mg$_{0.5}$Ti$_{0.5}$)O$_3$-modified tetragonal 0.875Bi$_{0.5}$Na$_{0.5}$TiO$_3$-0.125BaTiO$_3$ lead-free ferroelectric ceramics, J. Eur. Ceram. Soc. 38 (2018) 1381–1388.

[31] H. Qi, R.Z. Zuo, Giant electrostrictive strain in $(Bi_{0.5}Na_{0.5})TiO_3$-$NaNbO_3$ lead-free relaxor antiferroelectric featuring temperature and frequency stability, J. Mater. Chem. A 8 (2020) 2369–2375.

[32] M. Tyunina, A. Dejneka, D. Rytz, I. Gregora, F. Borodavka, M. Vondracek, J. Honolka, Ferroelectricity in antiferroelectric $NaNbO_3$ crystal, J. Phys.: Condens. Matter 26 (2014) 125901.

[33] A.W. Xie, H. Qi, R.Z. Zuo, A. Tian, J. Chen, S.J. Zhang, An environmentally-benign $NaNbO_3$-based perovskite antiferroelectric alternative to traditional Pb-based counterparts, J. Mater. Chem. C 7 (2019) 15153–15161.

[34] Y. Hiruma, H. Nagata, T. Takenaka, Phase diagrams and electrical properties of $(Bi_{1/2}Na_{1/2})TiO_3$-based solid solutions, J. Appl. Phys. 104 (2008) 124106.

[35] M.D. Peel, S.P. Thompson, A. Daoud-Aladine, S.E. Ashbrook, P. Lightfoot, New twists on the perovskite theme: Crystal structures of the elusive phases R and S of $NaNbO_3$, Inorg. Chem. 51 (2012) 6876–6889.

[36] B. Wylie-van Eerd, D. Damjanovic, N. Klein, N. Setter, J. Trodahl, Structural complexity of $(Na_{0.5}Bi_{0.5})TiO_3$-$BaTiO_3$ as revealed by Raman spectroscopy, Phys. Rev. B 82 (2010) 104112.

[37] K. Kakimoto, K. Akao, Y. Guo, H. Ohsato, Raman scattering study of piezoelectric $(Na_{0.5}K_{0.5})NbO_3$-$LiNbO_3$ ceramics, Jpn. J. Appl. Phys. 44 (2005) 7064–7067.

[38] D. Schütz, M. Deluca, W. Krauss, A. Feteira, T. Jackson, K. Reichmann, Lone–pair-induced covalency as the cause of temperature- and field-induced instabilities in bismuth sodium titanate, Adv. Funct. Mater. 22 (2012) 2285–2294.

[39] V.R. Mastelaro, H.R. Favarim, A. Mesquita, A. Michalowicz, J. Moscovici, J.A. Eiras, Local structure and hybridization states in $Ba_{0.9}Ca_{0.1}Ti_{1-x}Zr_xO_3$ ceramic compounds: correlation with a normal or relaxor ferroelectric character, Acta Mater 84 (2015) 164–171.

[40] M.X. Zhou, R.H. Liang, Z.Y. Zhou, S.G. Yan, X.L. Dong, Novel sodium niobate-based lead-free ceramics as new environment-friendly energy storage materials with high energy density, high power density, and excellent stability, ACS Sustainable Chem. Eng. 6 (2018) 12755–12765.

[41] A. Tian, R.Z. Zuo, H. Qi, M. Shi, Large energy-storage density in transition-metal oxide modified $NaNbO_3$-$Bi(Mg_{1/2}Ti_{2/3})O_3$ lead-free ceramics through regulating antiferroelectric phase structure, J. Mater. Chem. A 8 (2020) 8352–8359.